PHOTONICS Research

Spin-decoupled metalens with intensity-tunable multiple focal points

BINGSHUANG YAO,[1] XIAOFEI ZANG,[1,2,*] YANG ZHU,[1] DAHAI YU,[3] JINGYA XIE,[1,2] LIN CHEN,[1,2] SEN HAN,[1,4] YIMING ZHU,[1,2,5] AND SONGLIN ZHUANG[1]

[1]*Terahertz Technology Innovation Research Institute, Terahertz Spectrum and Imaging Technology Cooperative Innovation Center, Shanghai Key Laboratory of Modern Optical System, University of Shanghai for Science and Technology, Shanghai 200093, China*
[2]*Shanghai Institute of Intelligent Science and Technology, Tongji University, Shanghai 200092, China*
[3]*Focused Photonics (Hangzhou) Inc, Hangzhou 310052, China*
[4]*Suzhou H&L Instruments LLC, Suzhou 215123, China*
[5]*e-mail: ymzhu@usst.edu.cn*
Corresponding author: xfzang@usst.edu.cn

The control of spin electromagnetic (EM) waves is of great significance in optical communications. Although geometric metasurfaces have shown unprecedented capability to manipulate the wavefronts of spin EM waves, it is still challenging to independently manipulate each spin state and intensity distribution, which inevitably degrades metasurface-based devices for further applications. Here we propose and experimentally demonstrate an approach to designing spin-decoupled metalenses based on pure geometric phase, i.e., geometric metasurfaces with predesigned phase modulation possessing functionalities of both convex lenses and concave lenses. Under the illumination of left-/right-handed circularly polarized (LCP or RCP) terahertz (THz) waves, these metalenses can generate transversely/longitudinally distributed RCP/LCP multiple focal points. Since the helicity-dependent multiple focal points are locked to the polarization state of incident THz waves, the relative intensity between two orthogonal components can be controlled with different weights of LCP and RCP THz waves, leading to the intensity-tunable functionality. This robust approach for simultaneously manipulating orthogonal spin states and energy distributions of spin EM waves will open a new avenue for designing multifunctional devices and integrated communication systems.   © 2021 Chinese Laser Press

https://doi.org/10.1364/PRJ.420665

1. INTRODUCTION

Metasurfaces, which are the two-dimensional counterpart of metamaterials, have unprecedented capability to accurately control the amplitude, phase, and polarization of electromagnetic (EM) waves at subwavelength resolution [1,2]. Unlike conventional wavefront modulations based on the gradual phase accumulation along the propagation direction, the manipulation of wavefront based on metasurfaces is related to abrupt phase changes at planar antenna interfaces, opening a new window to design ultracompact (or ultrathin) devices that can outperform traditional bulky devices. Metasurfaces are divided into two categories: one is the resonant metasurfaces related to resonant phase (e.g., antenna resonance), while the other is the geometric metasurfaces associated with Pancharatnam–Berry phase (or geometric phase). Geometric metasurfaces consisting of anisotropic antennas with identical shapes and different in-plane orientations are usually applied to design flat components to manipulate the spin EM waves, e.g., left-/right-handed circularly polarized (LCP or RCP) EM waves. Benefiting from the local control of the wavefronts of spin EM waves, geometric metasurfaces enable a plethora of applications including generalized Snell's law [3–5], metalenses [6–14], holograms [15–24], the spin Hall effect [25–28], polarization convertors [29–32], vortex beams [33–37], and nonlinear photonics [38–40].

The control of the wavefronts (e.g., amplitudes, phases, and polarizations) of spin EM waves is very important in optical communications [41,42]. With the increase of communication capacity, the independent manipulation of multiple spin beams with controllable energy allocation enables practical applications in multiple-target detection radar system and multiple-input multiple-output (MIMO) communications [43,44]. Additionally, miniaturization and integration are inevitable trends in the development of modern communication systems, and thus geometric metasurfaces provide a flexible platform to design the corresponding ultracompact devices/systems (for manipulating spin EM waves). Recently, great progress has been made on the independent manipulation of each spin state and energy distribution of spin EM waves [45–49]. For exam-

ple, Liu *et al.* proposed an approach using full Fourier components to design energy-tailorable spin-selective metasurfaces that can edit the energy configuration with a spin-selective behavior [43]. Based on the interference of dual geometric phases, Ding *et al.* designed a metasurface to demonstrate direct routing of intensity-editable multibeams [47]. On the other hand, by combining geometric phase and propagation/dynamic phase, the spin-decoupled metasurfaces can be designed to independently modulate spin states of EM waves. For instance, Xu *et al.* proposed a spin-decoupled phase control method for deflecting LCP and RCP output components toward different angles [48], while Yuan *et al.* designed a full phase-modulated metasurface to demonstrate an energy-editable circular polarization router [49]. Although the spin EM waves with intensity-editable functionality (which means that a designed metasurface has a fixed intensity ratio between two orthogonal spin EM beams or multiple beams) have been experimentally reported in previous works, the independent manipulation of two orthogonal spin EM beams with intensity-tunable functionality (arbitrary and continuously controllable intensity ratio between two orthogonal spin EM beams) has not yet been demonstrated to the best of our knowledge. Here, unlike the previous spin-decoupling approach depending on joint modulation (geometric phase combined with propagation phase) or designing multiple metasurfaces (to achieve different intensity ratios between two orthogonal spin EM beams), an approach based on the pure geometric phase is proposed to design a spin-decoupled metalens that can independently modulate each spin state and intensity ratio of spin EM waves (based on one single geometric metasurface), leading to a spin-decoupled metalens with intensity-tunable multiple focal points. Such a spin-decoupled metalens is designed by integrating the functionalities of multiple convex lenses and concave lenses into a single metasurface. Under the illumination of LCP (or RCP) THz waves, this metalens can focus the incident THz waves into multiple RCP (or LCP) focal points, leading to the helicity-dependent multiple focal points. The intensity ratio between LCP and RCP multiple focal points can be arbitrarily controlled by different weights of LCP/RCP incident THz waves. The robust and unique approach in controlling spin state and energy distribution of spin EM waves may open an avenue for designing multifunctional devices and integrated systems.

2. DESIGN AND METHOD

A terahertz (THz) spin-decoupled metalens is schematically shown in Fig. 1. This metalens consists of a variety of microrods with identical shape but different orientations sitting on a silicon substrate, and thus the manipulation of incident THz waves is dependent on pure geometric phase. For the incidence of LCP THz waves, such a metalens can generate two RCP focal points with the same focal distance (or different focal distance) that are transversely distributed (or longitudinally distributed) in the propagation direction (see Fig. 1). In contrast, there are two LCP focal points [that are transversely distributed (or longitudinally distributed) in the propagation direction] that can be observed under the illumination of RCP THz waves. In fact, our designed geometric metalens enables spin-decoupling functionality that can focus both LCP and
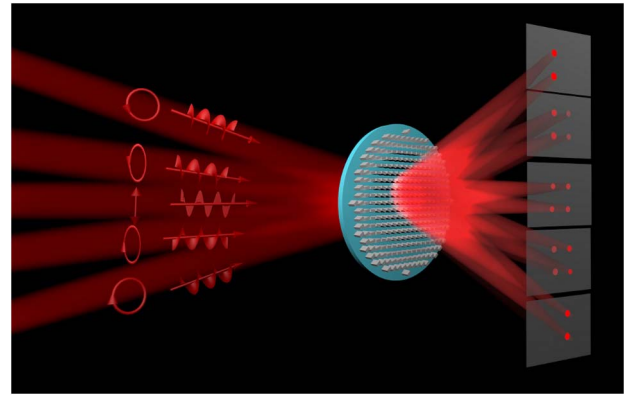

Fig. 1. Schematic of the spin-decoupled metalens with intensity-tunable multiple focal points. Under the illumination of LCP THz waves, two RCP focal points are generated, while two LCP focal points can be observed for the incident RCP THz waves. The intensity between two RCP focal points and two LCP focal points can be arbitrarily modulated with different weights of LCP and RCP incident THz waves.

RCP THz waves into helicity-dependent multiple focal points. It should be noted that all of the multiple RCP and LCP focal points are locked to the polarization state of incident THz waves. Therefore, the intensity of the helicity-dependent multiple focal points can be arbitrarily allocated by controlling the ellipticity of incident THz waves (see Fig. 1). For a geometric metalens that can focus LCP EM waves into a focal point, the required phase modulation can be governed by

$$\varphi_{\text{LCP}} = \frac{2\pi}{\lambda}\sqrt{(x-x_L)^2 + (y-y_L)^2 + f_L^2} - f_L, \quad (1)$$

in which λ is the working wavelength and f_L is the focal length. The generated RCP focal point is located at (x_L, y_L, f_L) in theory, and (x_L, y_L) is an arbitrary coordinate in the $x - y$ plane.

If a geometric metalens can focus the LCP incident EM waves into multiple focal points, the required geometric phase can be written as

$$\varphi_{\text{LCP}}^n = \sum_{i=1}^{n}\left[\frac{2\pi}{\lambda}\sqrt{(x-x_i)^2 + (y-y_i)^2 + f_i^2} - f_i\right], \quad (2)$$

where the incident EM waves are focused into n focal points and the ith RCP focal point is distributed at (x_i, y_i, f_i).

In contrast, when a geometric metalens is applied to focus the RCP EM waves into multiple focal points, the phase profile for such a metalens can be expressed as

$$\varphi_{\text{RCP}}^m = -\sum_{j=1}^{m}\left[\frac{2\pi}{\lambda}\sqrt{(x-x_j)^2 + (y-y_j)^2 + f_j^2} - f_j\right], \quad (3)$$

where the jth LCP focal point is distributed at (x_j, y_j, f_j).

In fact, if a geometric metalens can simultaneously modulate LCP and RCP EM waves to generate both RCP and LCP multiple focal points, the total phase profile is given as follows:

$$\varphi_{\text{total}} = \arg[\exp(i\varphi_{\text{LCP}}^n) + \exp(i\varphi_{\text{RCP}}^m)], \quad (4)$$

in which the phase modulation can focus the incident LCP/RCP EM waves into n/m RCP/LCP focal points.

It should be noted that the total phase requirements in Eq. (4) contain two independent phase profiles: one is the phase profile that can focus the LCP component into multiple RCP focal points, while the other is the phase profile that can focus the RCP component into multiple LCP focal points. Therefore, a spin-decoupled metalens with the aforementioned function [see Eq. (4)] is realized by embedding the functionalities of multiple convex lenses and concave lenses into a single metasurface, i.e., the LCP (RCP) EM waves will "see" n convex lenses and m concave lenses (m convex lenses and n concave lenses) under the modulation of phase profile in Eq. (4).

Figure 2(a) shows a schematic of the spin-decoupled metalens consisting of a variety of anisotropic silicon microrods with predesigned in-plane orientations. The unit cell is shown in Fig. 2(b), and the structure parameters are optimized as $L = 99$ μm, $W = 35$ μm, $h_1 = 500$ μm, and $p = 120$ μm (period). The thickness of silicon-based substrate is $h_2 = 500$ μm. As depicted in Fig. 2(c), a unit cell with the long axis along the x axis is interacting with transverse-electric (TE) and transverse-magnetic (TM) THz waves, and the corresponding transmission spectra show strong oscillations. Therefore, the anisotropic microrod with substrate can be considered a hybrid Fabry–Perot resonator (like in Ref. [8]). The transmissivities of both the TE and TM THz waves at $f = 0.6$ THz are the same ($T = 90\%$), while the phase retardation between the TE and TM transmitted waves is 175° ($\approx\pi$) [see Fig. 2(d)]. As a consequence, the designed microrod can be considered as a quasi-perfect half-wave plate (at $f = 0.6$ THz), and thus the incident circularly-polarized (CP) EM waves (interacting with the microrod) will be converted into CP EM waves with orthogonal polarization and an additional phase delay of $\pm2\theta$ (θ is the rotating angle between the x axis and the long side of the microrod; "+" and "−" represent the sign of the phase shift

for the incident RCP and LCP light, respectively). Figures 2(e) and 2(f) show the two fabricated samples to generate four transversely [see Fig. 2(e)] and longitudinally [see Fig. 2(f)] distributed helicity-dependent focal points, respectively. In order to experimentally demonstrate the properties of the designed metalenses, near-field scanning THz microscopy (NSTM) is used to detect the corresponding electric-field distributions.

3. RESULTS

As a feasibility study, we first discuss the spin-decoupled metalens that can generate helicity-dependent multiple focal points with the same focal distance. Numerical simulations and experimental demonstrations of such a metalens are shown in Fig. 3. To verify our proposed approach, a metalens consisting of 100×100 microrods (with different in-plane orientations) is designed to generate the required phase profile. The work frequency is 0.6 THz. The focusing parameters of these helicity-dependent multiple focal points are predesigned as follows: $x_L^1 = x_L^2 = 1.5$ mm, $x_R^1 = x_R^2 = -1.5$ mm, $y_L^1 = y_L^2 = -1.5$ mm, $y_L^1 = y_L^2 = 1.5$ mm, and $f_L^1 = f_L^2 = f_R^1 = f_R^2 = 4.0$ mm. In theory, such a spin-decoupled metalens can generate two RCP (LCP) focal points located at (1.5, 1.5, 4.0 mm) and (1.5, −1.5, 4.0 mm) [(−1.5, 1.5, 4.0 mm) and (−1.5, −1.5, 4.0 mm)], under the illumination of LCP (RCP) THz waves. Figure 3(a1) shows the simulated electric-field intensity ($|E|^2$) distribution of our designed metalens upon the incidence of LCP THz waves (with ellipticity $\chi = 1.0$). There are two RCP focal points that can be observed after the metalens. One focal point is nearly located at (1.5, 1.5, 3.75 mm), while the other one is nearly at (1.5, −1.5, 3.75 mm). Here, the discrepancy in focal distance between the theoretical design and numerical simulation can be attributed
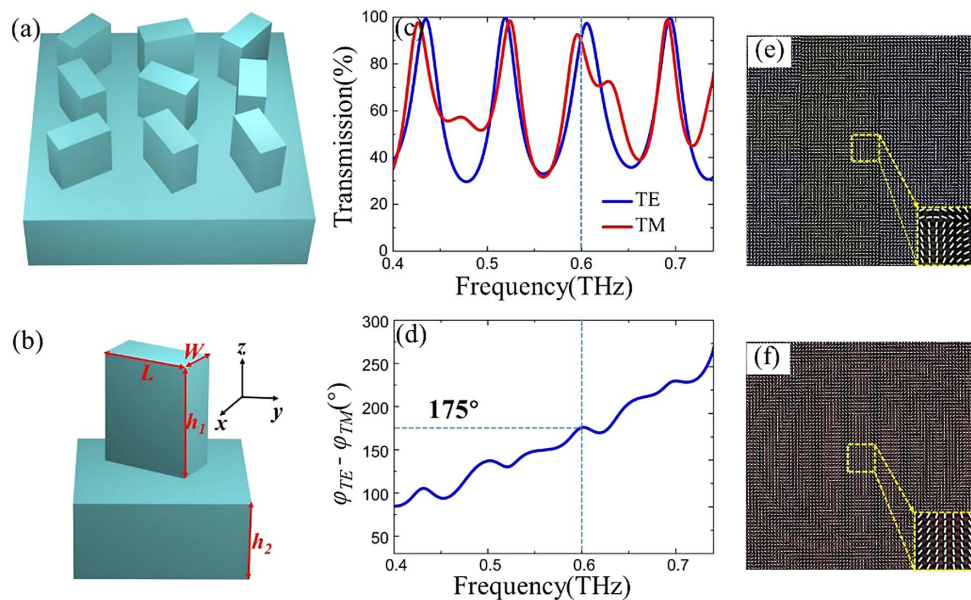

Fig. 2. Schematic, principle, and fabrication of the spin-decoupled metalens. (a) Schematic of the spin Hall metalens consisting of a variety of silicon microrods with identical shape but different orientations. (b) Unit cell of the microrod. (c) The transmission spectra of microrods under the illumination of TE and TM THz waves. (d) The corresponding phase difference between the transmitted TE and TM THz waves. (e) and (f) Optical images of the fabricated spin-decoupled metalenses that can generate transversely distributed and longitudinally distributed RCP and LCP multiple focal points, respectively.
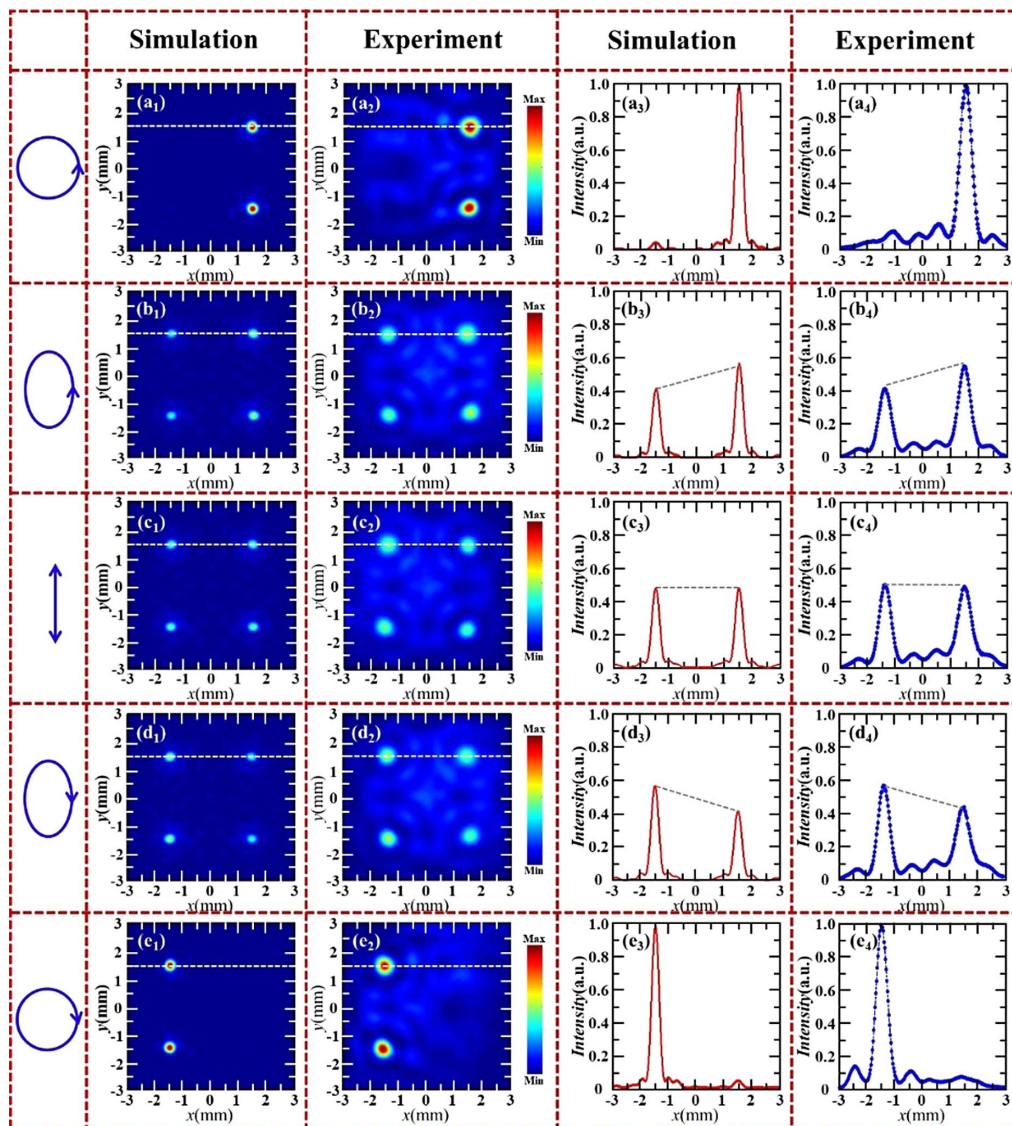
Fig. 3. Electric-field intensity distributions ($|E|^2$) for the spin-decoupled metalens that can generate transversely distributed multiple focal points. (a1), (a2), (b1), (b2), (c1), (c2), (d1), (d2), and (e1), (e2) are the corresponding electric-field intensity distributions at the $x - y$ plane ($z = 3.75$ mm) for the incidence of LCP, LECP, LP, RECP, and RCP THz waves, respectively. (a3), (a4), (b3), (b4), (c3), (c4), (d3), (d4), and (e3), (e4) are the corresponding electric-field intensity distributions at line $y = 1.5$ mm ($z = 3.75$ mm) for the incidence of LCP, LECP, LP, RECP, and RCP THz waves, respectively.

to the nonperfect half-wave plate of each microrod. The experimental measurement is shown in Fig. 3(a2). Under the illumination of LCP THz waves, the fabricated metalens [see Fig. 2(e)] can also modulate the incident THz waves into two focal points, and they are located at (1.5, 1.5, 3.75 mm) and (1.5, −1.5, 3.75 mm), respectively. In comparison with Figs. 3(a1) and 3(a2), the experimental measurement is well matched with the numerical simulation, except for a slight deviation (i.e., different sizes between numerical and measured focal points) that can be ascribed to fabrication errors and testing errors. Figures 3(a3) and 3(a4) show the calculated and measured electric-field intensity along $y = 1.5$ mm, and one peak with normalized intensity of $T = 1$ is observed nearly at $x = 1.5$ mm. When the incident THz beam is switched into a left-handed elliptically polarized (LECP) THz beam (with

ellipticity $\chi = 0.152$), the spin-decoupled metalens can generate two more focal points as shown in Figs. 3(b1) and 3(b2). In addition to the original two RCP focal points nearly located at (1.5, 1.5, 3.75 mm) and (1.5, −1.5, 3.75 mm), there are another two LCP focal points generated nearby at (−1.5, 1.5, 4 mm) and (−1.5, −1.5, 4 mm), respectively. The normalized electric-field intensities of the upper left and right focal points are 0.42 and 0.58, respectively [see Figs. 3(b3) and 3(b4)]. For the incidence of linearly polarized (LP) THz waves (with ellipticity $\chi = 0$), there are still four focal points that can be observed [see Figs. 3(c1) and 3(c2)], but the electric-field intensity ratio between the left and right two focal points is 0.5:0.5 [see Figs. 3(c3) and 3(c4)]. The electric-field intensity ratio between the left and right two focal points is flipped to 0.58:0.42, when the right-handed elliptically polarized (RECP)
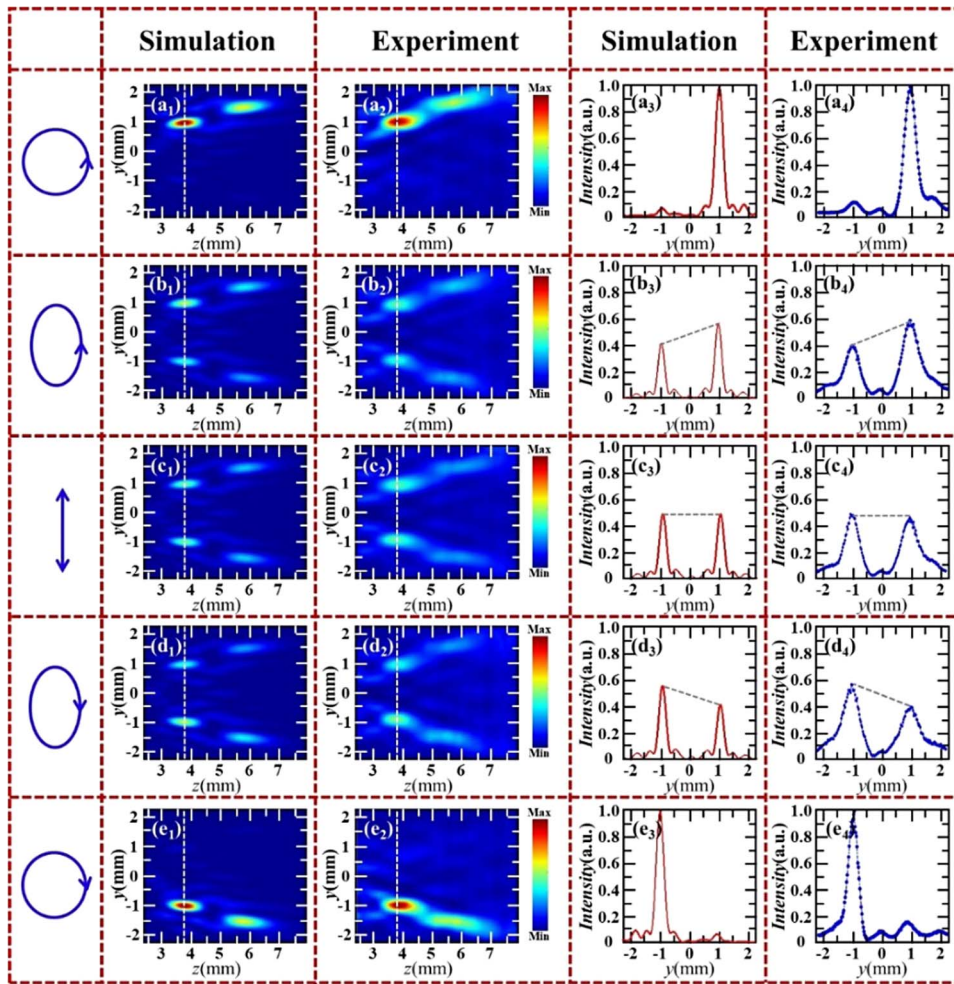
Fig. 4. Electric-field intensity distributions ($|E|^2$) for the spin-decoupled metalens that can generate longitudinally distributed multiple focal points. (a1), (a2), (b1), (b2), (c1), (c2), (d1), (d2), and (e1), (e2) are the corresponding electric-field intensity distributions at the x–z plane ($y = 0$ mm) for the incidence of LCP, LECP, LP, RECP, and RCP THz waves, respectively. (a3), (a4), (b3), (b4), (c3), (c4), (d3), (d4), and (e3), (e4) are the corresponding electric-field intensity distributions at line $z = 3.75$ mm for the incidence of LCP, LECP, LP, RECP, and RCP THz waves, respectively.

THz waves with ellipticity $\chi = -0.152$ interact with the metalens [see Figs. 3(d1)–3(d4)]. In addition, under the illumination of RCP THz waves (with ellipticity $\chi = -1.0$), the two focal points in the right side disappear, while the left two focal points with normalized intensity of $T = 1$ can be observed as shown in Figs. 3(e1)–3(e4). The simulated focusing efficiency of the designed spin-decoupled metalens is 32.8%, while the measured focusing efficiency is 24.5%. The low focusing efficiency of the fabricated metalens can be attributed to the intrinsic limitation (the approach of pure geometric phase to design the spin-decoupled metalens), and fabrication errors, i.e., collapse/loss of rods and unmatched size between the fabricated and designed rod. In order to further enhance the working efficiency, we need to improve the fabrication accuracy (to reduce the fabrication errors) and carefully select quality materials, e.g., TiO_2, GaN, like in Refs. [9,50]. As a summary, the intensity ratio between two RCP and two LCP focal points can be flexibly controlled by changing the weights of the LCP and RCP THz waves, that is, the designed spin-decoupled metalens enabling intensity-tunable functionality. Under the

illumination of THz waves with different polarization states, the calculated and measured electric-field intensity distributions along line $y = -1.5$ mm ($z = 3.75$ mm) are shown in Appendix A, while the calculated and measured electric-field intensity distributions in the x–z plane are supplied in Appendix B. The calculated electric-field intensities at focal plane with different ellipticity are given in Appendix C. The sizes of the focal points and focal lengths are supplied in Appendix D (see Tables 1 and 2).

The proposed approach cannot only modulate the incident THz waves into transversely distributed multiple focal points but also enables the capability to steer the THz waves to form longitudinally distributed multiple focal points with intensity-tunable functionality. Figure 4 shows the calculated and measured results. The structure parameters of such a metalens for focusing longitudinally distributed multiple focal points are as follows: $x_L^1 = x_L^2 = x_R^1 = x_R^2 = 0$ mm, $y_L^1 = -y_R^1 = 1.0$ mm, $y_L^2 = -y_R^2 = 1.5$ mm, $f_L^1 = f_R^1 = 4.0$ mm, and $f_L^2 = f_R^2 = 6.0$ mm. Therefore, there are two longitudinally distributed RCP focal points that can be observed at (0, 1.0, 4.0 mm)

and (0, 1.5, 6.0 mm), under the illumination of LCP THz waves, while two longitudinally distributed LCP focal points are generated at (0, –1.0, 4.0 mm) and (0, –1.5, 6.0 mm), under the illumination of RCP THz waves. Figure 4(a1) shows the calculated electric-field intensity distribution of the designed metalens for the incidence of LCP THz waves. Two RCP focal points are observed after the metalens, and one is located at (0, 1.0, 3.75 mm), while the other is distributed at (0, 1.5, 5.7 mm). In an experiment, these two RCP focal points can also be detected as shown in Fig. 4(a2). The calculated and measured electric-field distributions at line $z = 3.75$ mm ($x = 0$ mm) are shown in Figs. 4(a3) and 4(a4), and only one peak with normalized transmission ($T = 1$) at $y = 1.0$ mm can be observed. In comparison with Figs. 4(a1) [or 4(a3)] and 4(a2) [or 4(a4)], the numerical simulations agreed well with the measurement results. When the incident LCP THz waves are switched into LECP THz waves with ellipticity of $\chi = 0.152$, two more LCP focal points are generated at (0, –1.0, 3.75 mm) and (0, –1.5, 5.7 mm), respectively [see Figs. 4(b1) and 4(b2)]. The electric-field distributions at line $z = 3.75$ mm demonstrate that the normalized intensity ratio between RCP and LCP focal points is 0.58:0.42. In addition, for the incidence of LP (with $\chi = 0$), RECP (with $\chi = -0.152$), and RCP (with $\chi = -1.0$) THz waves, the normalized intensity ratios between RCP and LCP focal points are 0.5:0.5, 0.42:0.58, and 0:1, respectively, demonstrating the intensity-tunable functionality of the designed metalens [see Figs. 3(c1)–3(e4)]. The simulated focusing efficiency of this spin-decoupled metalens is 32.5%, while the measured focusing efficiency is 21.8%. The sizes of the focal points and focal lengths are supplied in Appendix D (see Tables 3 and 4). The electric-field distributions at line $z = 5.7$ mm ($x = 0$ mm) are shown in Appendix E, and the electric-field distributions at the $x - y$ plane ($z = 3.75$ mm and $z = 5.7$ mm) are given in Appendix F and Appendix G. The calculated electric-field intensities at the focal plane with different ellipticity are supplied in Appendix H.

4. DISCUSSION AND CONCLUSION

Geometric phase-based (or Pancharatnam–Berry phase-based) metasurfaces (named geometric metasurfaces) enable an unprecedented capability to control the phase, polarization, and amplitude of circularly polarized EM waves by arranging the orientation angle (θ) of each anisotropic antenna. Geometric metasurfaces with predesigned phase profiles are robust against fabrication tolerance (antenna size and roughness) and material property variations. However, the inherent conjugated symmetry, i.e., equal and opposite phase distributions under the illumination of LCP and RCP EM waves, inevitably hinders geometric metasurfaces from implementing spin-decoupled/switchable functionalities. To overcome this limitation, the traditional approach is to combine the geometric phase and propagation phase (or dynamic phase) together to decouple the spin-locking between two helicity components. As demonstrated in Ref. [51], the independent manipulation of chiral holograms is realized based on both geometric phase and propagation phase. A THz spin-decoupled bifunctional metacoupler was proposed and numerically demonstrated for

independently deflecting/manipulating LCP and RCP components, i.e., simultaneously generating anomalous reflection and converting the incident waves into SPPs (surface plasmon polaritons) [52]. Furthermore, the independent manipulation of two orthogonal spin components with applications in generating spin-coupled multiple focal points, orbital angular momentum (OAM) vortices, anomalous refraction, beam splitters, and holograms has been demonstrated [53–58]. In the same way, Zhang *et al*. designed the spin-decoupled metasurfaces (based on propagation and geometric phases) to independently manipulate the two (incident) orthogonal helicity components, and thus the switchable functionalities and the simultaneous generation of separate multiple integer and fractional OAM modes occupying both copolarized and cross-polarized output channels were also realized [59,60]. Another approach to design polarization-controlled metasurfaces is based on pure propagation phase. For example, Boroviks *et al*. and Yin *et al*. proposed gap surface plasmon-based metasurfaces and hyperbolic metasurfaces to independently control the x-polarized and y-polarized EM waves. By accurately designing the structure of each unit cell (with different sizes) to match the predesigned phase requirement (which can be considered propagation phase), the polarization-controlled focal points can be generated [61,62]. However, the traditional method (the pure propagation phase or the combining of geometric phase and propagation phase) that can independently manipulate two orthogonal helicity components (or x-polarized and y-polarized EM waves) inevitably needs to perform the scanning of a large number of parameters to achieve the desired unit cells (a variety of meta-atoms with different sizes to match the propagation phase requirement). Metasurfaces with planar chiral meta-atoms or chiral geometric metasurfaces can also decouple the spin-locking between two orthogonal helicity components [63–65]. Based on the chiral atoms (or chiral phase), geometric phase, and propagation phase, Chen *et al*. [63] and Yuan *et al*. [64] demonstrated the spin-independent holograms and the independent phase modulation functionality in four channels. All of these two works also relied on both propagation and geometric phases, and thus scanning of a large number of parameters to achieve the desired unit cells is inevitable. In addition, Chen *et al*. designed plasmonic chiral geometric metasurfaces to realize spin-independent holograms. But this approach is limited to fabricating complicated and stepped nanoapertures in comparison with our single-layer metalens [65]. In fact, we have proposed an approach to design spin-decoupled metalenses based on the pure geometric phase. This method has obvious advantages in the simplicity of designing spin-decoupled metasurfaces (without scanning a large number of parameters) that can independently manipulate two orthogonal helicity components. For the designed metalenses, the intensity ratio between helicity-dependent focal points can be continuously allocated by switching the polarization of incident THz waves from LCP to RCP. However, the target phase in Eq. (4) consists of two convex lenses and two concave lenses (resulting in a diverging beam), and the maximal focusing efficiency of the designed metalens cannot exceed 50% in theory, which is an intrinsic limitation (disadvantage) of our proposed approach. In a word, the approach demonstrated in this work

provides a flexible platform (with obvious advantages in the simplicity of designing spin-decoupled metasurfaces based on pure geometric phase) that can independently and continuously allocate intensity ratio between helicity-dependent focal points, but at the cost of losing working efficiency.

In summary, we have proposed an approach to design a spin-decoupled metalens that can independently modulate two orthogonal spin states of spin THz waves based on pure geometric phase. As a multifocus metalens, the incident LCP (or RCP) THz waves could be focused into helicity-dependent multiple focal points. The transversely distributed (or longitudinally distributed) helicity-dependent multiple focal points were experimentally demonstrated, and the intensity ratios between the RCP and LCP multiple focal points were arbitrarily allocated by selecting different weights of LCP and RCP THz waves. The robust and flexible approach in manipulating spin EM waves may have potential applications in designing multifunctional devices and integrated communication systems.

APPENDIX A: ELECTRIC-FIELD INTENSITY DISTRIBUTIONS ($|E|^2$) OF A SPIN-DECOUPLED METALENS AT LINE $y = -1.5$ mm ($z = 3.75$ mm)

Figure 5 shows the corresponding electric-field distributions at line $y = -1.5$ mm ($z = 3.75$ mm), under the illumination of LCP, LECP, LP, RECP, and RCP THz waves. For the incidence of LCP ($\chi = 1.0$) THz waves, one peak (with normalized transmission $T = 1$) near $x = 1.5$ mm is observed [see the calculated and measured results in Figs. 5(a1) and 5(b1)]. When the polarization of incident THz waves is switched to LECP ($\chi = 0.152$), two peaks located at $x = 1.5$ mm and $x = -1.5$ mm are observed. The normalized intensities between these two peaks are 0.42 and 0.58, respectively [see Figs. 5(a2) and 5(b2)]. The relative intensity ratio of these two peaks is changed to 0.5:0.5 for the incidence of LP ($\chi = 0$) THz waves [see Figs. 5(a3) and 5(b3)]. The normalized intensities between these two peaks are flipped (0.58:0.42)

for the incidence of RECP ($\chi = -0.152$) THz waves [see Figs. 5(a4) and 5(b4)]. In contrast, only one peak (with normalized transmission $T = 1$) near $x = -1.5$ mm is observed, under the illumination of RCP ($\chi = -1.0$) THz waves [see Figs. 5(a5) and 5(b5)].

APPENDIX B: ELECTRIC-FIELD INTENSITY DISTRIBUTIONS ($|E|^2$) AT THE $x - z$ PLANE

Figure 6 shows the calculated and measured electric-field distributions at the $x - z$ plane for the spin-decoupled metalens that can generate transversely distributed multiple focal points. As shown in Fig. 6(a1), one focal point located at (1.5, 1.5, 3.75 mm) is observed at the $x - z$ plane ($y = 1.5$ mm). The measured electric-field distribution shown in Fig. 6(a2) is matched well with the numerical simulation [in Fig. 6(b1)]. For the incidence of LECP ($\chi = 0.152$), LP ($\chi = 0$), and RECP ($\chi = -0.152$) THz waves, another focal point appears at (-1.5, 1.5, 3.75 mm) [see Figs. 6(a2)–6(a4) and Figs. 6(b2)–6(b4)]. Under the illumination of THz waves with the polarization switched from LCP to RCP, only one focal point located at (-1.5, 1.5, 3.75 mm) can be observed [see Figs. 6(a5) and 6(b5)]. As depicted in Figs. 6(a1)–6(b5), the intensity of the focal point located at the upper half space becomes weaker and weaker, while the intensity of the focal point located at the upper half space gets stronger and stronger when the incident THz waves with polarization gradually switched from LCP to RCP. Figures 6(c1)–6(d5) show the corresponding electric-field distributions at the $x - z$ plane ($y = -1.5$ mm). For the incidence of LCP ($\chi = 1.0$), LECP ($\chi = 0.152$), LP ($\chi = 0$), RECP ($\chi = -0.152$), and RCP ($\chi = -1.0$) THz waves, the intensity-tunable functionality between helicity-dependent focal points is also demonstrated [see Figs. 6(c1)–6(d5)]. Therefore, the designed spin-decoupled metalens enables unprecedented capability that can focus the incident spin THz waves into multiple helicity-dependent focal
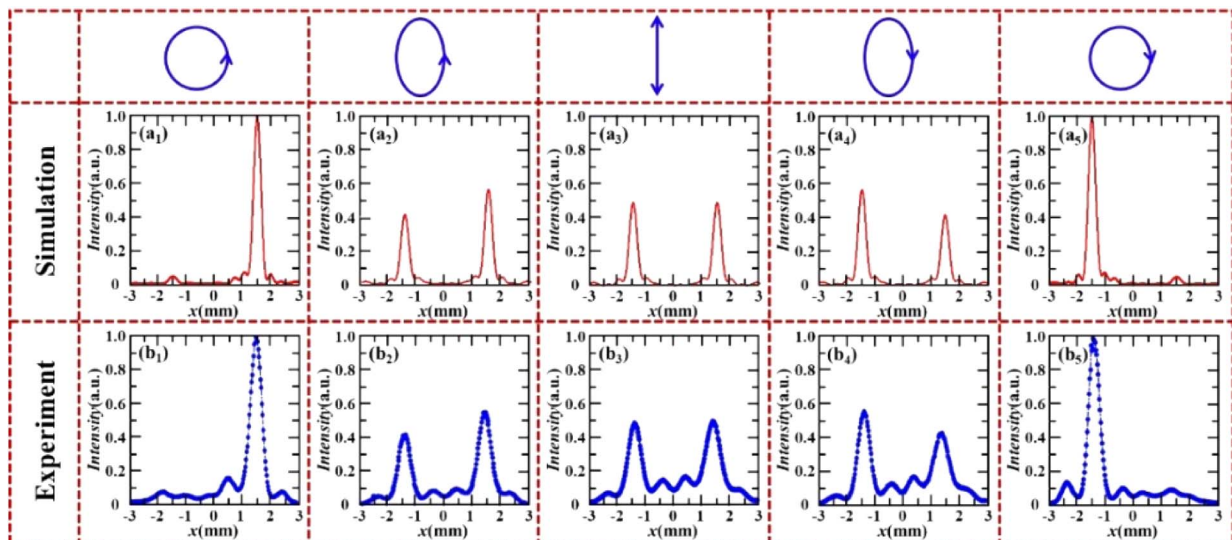

Fig. 5. Calculated and measured electric-field intensity distributions at line $y = -1.5$ mm ($z = 3.75$ mm) for the incidence of (a1), (b1) LCP, (a2), (b2) LECP, (a3), (b3) LP, (a4), (b4) RECP, and (a5), (b5) RCP THz waves.
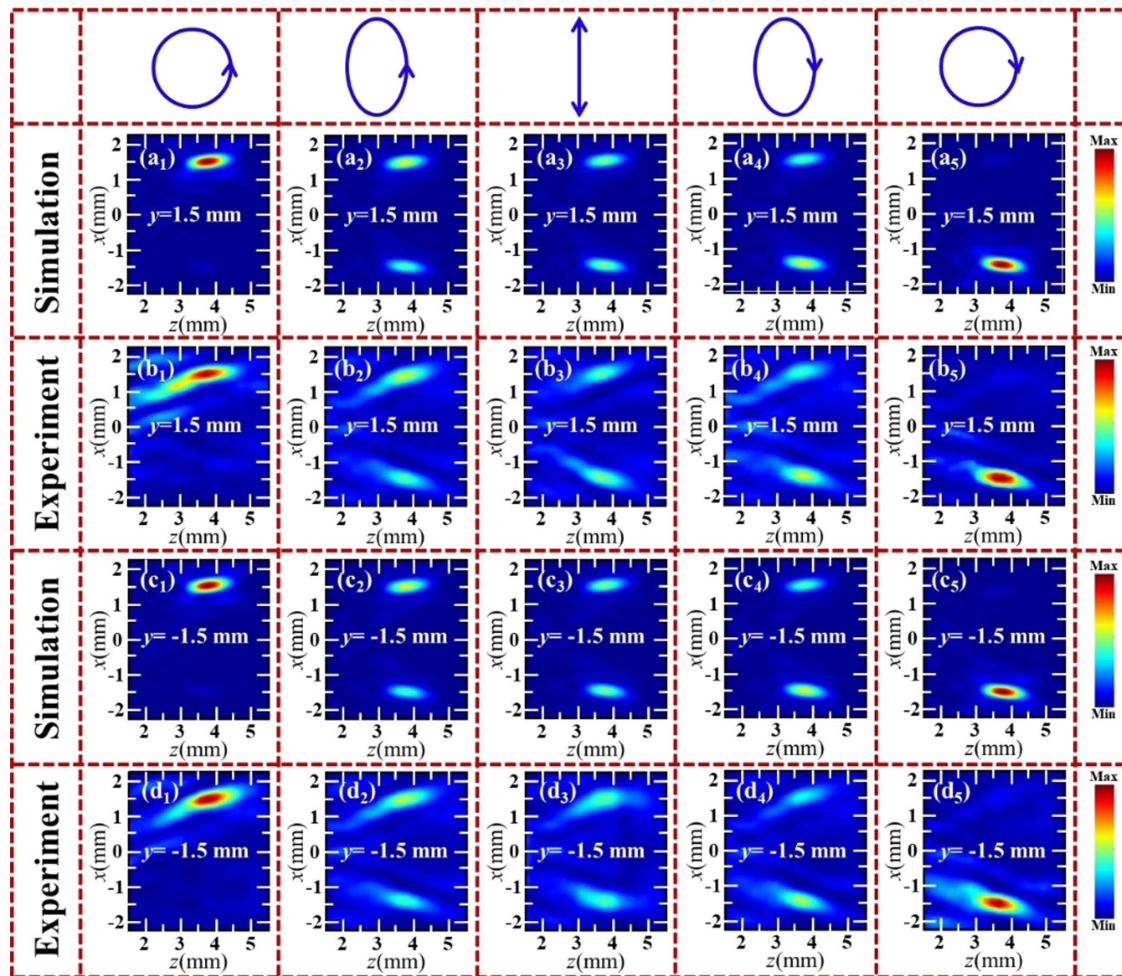
Fig. 6. Electric-field intensity distributions (under the illumination of THz waves with polarization switched from LCP to RCP) at the $x - z$ plane for the spin-decoupled metalens that can generate transversely distributed multiple focal points.

points and flexibly control the intensity ratio between the helicity-dependent multiple focal points.

APPENDIX C: SIMULATED ELECTRIC-FIELD INTENSITIES ($|E|^2$) AT THE FOCAL PLANE

Figure 7 shows the calculated electric-field intensities at the focal plane under the illumination of THz waves with different polarization states. As shown in Fig. 7(a) (red curve) for the incidence of THz waves with ellipticity gradually switched from $+1$ to -1, the normalized electric-field intensity ($|E|^2$) at point (1.5, 1.5, 3.75 mm) is gradually decreased from 1 to 0. In contrast, the normalized electric-field intensity ($|E|^2$) at point (1.5, 1.5, 3.75 mm) is gradually increased from 0 to 1, when the ellipticity of the incident THz waves is gradually switched from
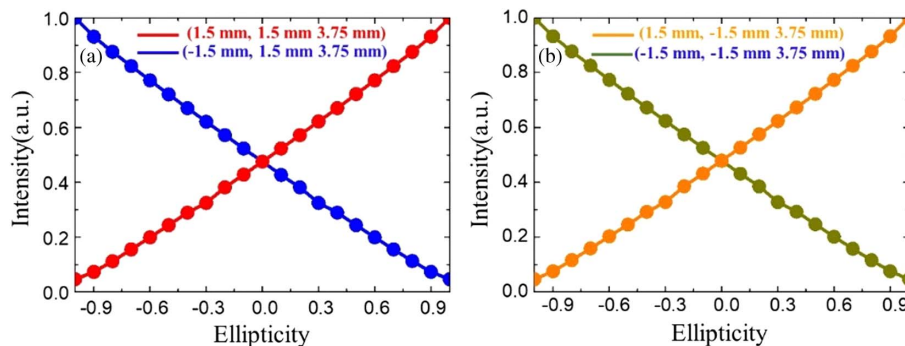

Fig. 7. Simulated electric-field intensities ($|E|^2$) at the focal plane. (a) The electric-field intensities ($|E|^2$) at point (1.5, 1.5, 3.75 mm) (red curve) and point (-1.5, 1.5, 3.75 mm) (blue curve) with different ellipticity of the THz waves. (b) The electric-field intensities ($|E|^2$) at point (1.5, -1.5, 3.75 mm) (orange curve) and point (-1.5, -1.5, 3.75 mm) (dark yellow curve) with different ellipticity of the THz waves.

+1 to –1 as shown in Fig. 7(a) (blue curve). The corresponding electric-field intensities at point (1.5, –1.5, 3.75 mm) and point (–1.5, –1.5, 3.75 mm) for the incidence of THz waves (with ellipticity gradually switched from +1 to –1) are shown in Fig. 7(b). The intensity-tunable functionality between two orthogonal helicity-dependent focal points is also demonstrated by controlling the weights of LCP and RCP incident THz waves.

APPENDIX D: SIZES OF FOCAL POINTS AND FOCAL LENGTH

Table 1. Sizes of the Focal Points of the Metalens for Generating Transversely Distributed Multiple Focal Points

	Focal Position (mm)	LCP ($\chi = 1.0$)	LECP ($\chi = 0.152$)	LP ($\chi = 0$)	RECP ($\chi = -0.152$)	RCP ($\chi = -1.0$)
Simulation	(1.5, 1.5, 3.75)	310 µm	320 µm	320 µm	320 µm	N/A
	(–1.5, 1.5, 3.75)	N/A	320 µm	320 µm	320 µm	310 µm
Experiment	(1.5, 1.5, 3.75)	500 µm	545 µm	550 µm	535 µm	N/A
	(–1.5, 1.5, 3.75)	N/A	525 µm	615 µm	600 µm	500 µm
Simulation	(1.5, –1.5, 3.75)	305 µm	325 µm	320 µm	320 µm	N/A
	(–1.5, –1.5, 3.75)	N/A	320 µm	320 µm	320 µm	305 µm
Experiment	(1.5, –1.5, 3.75)	485 µm	560 µm	550 µm	535 µm	N/A
	(–1.5, –1.5, 3.75)	N/A	575 µm	625 µm	625 µm	500 µm

Table 2. Focal Length of the Metalens for Generating Transversely Distributed Multiple Focal Points

	Focal Position (mm)	LCP ($\chi = 1.0$)	LECP ($\chi = 0.152$)	LP ($\chi = 0$)	RECP ($\chi = -0.152$)	RCP ($\chi = -1.0$)
Simulation	(1.5, 1.5, 3.75)	905 µm	910 µm	910 µm	915 µm	N/A
	(–1.5, 1.5, 3.75)	N/A	905 µm	910 µm	910 µm	900 µm
Experiment	(1.5, 1.5, 3.75)	1355 µm	1290 µm	1290 µm	1255 µm	N/A
	(–1.5, 1.5, 3.75)	N/A	1300 µm	1270 µm	1185 µm	1155 µm
Simulation	(1.5, –1.5, 3.75)	905 µm	910 µm	910 µm	910 µm	N/A
	(–1.5, –1.5, 3.75)	N/A	900 µm	910 µm	915 µm	905 µm
Experiment	(1.5, –1.5, 3.75)	1260 µm	1255 µm	1330 µm	1305 µm	N/A
	(–1.5, –1.5, 3.75)	N/A	1285 µm	1310 µm	1225 µm	1170 µm

Table 3. Sizes of the Focal Points of the Metalens for Generating Longitudinally Distributed Multiple Focal Points

	Focal Position (mm)	LCP ($\chi = 1.0$)	LECP ($\chi = 0.152$)	LP ($\chi = 0$)	RECP ($\chi = -0.152$)	RCP ($\chi = -1.0$)
Simulation	(0, 1.0, 3.75)	305 µm	280 µm	280 µm	275 µm	N/A
	(0, 1.5, 5.70)	370 µm	350 µm	345 µm	340 µm	N/A
Experiment	(0, 1.0, 3.75)	480 µm	635 µm	605 µm	680 µm	N/A
	(0, 1.5, 5.70)	590 µm	720 µm	725 µm	710 µm	N/A
Simulation	(0, –1.0, 3.75)	N/A	280 µm	280 µm	280 µm	305 µm
	(0, –1.5, 5.70)	N/A	345 µm	345 µm	345 µm	370 µm
Experiment	(0, –1.0, 3.75)	N/A	625 µm	580 µm	725 µm	485 µm
	(0, –1.5, 5.70)	N/A	715 µm	710 µm	765 µm	565 µm

Table 4. Focal Length of the Metalens for Generating Longitudinally Distributed Multiple Focal Points

	Focal Position (mm)	LCP ($\chi = 1.0$)	LECP ($\chi = 0.152$)	LP ($\chi = 0$)	RECP ($\chi = -0.152$)	RCP ($\chi = -1.0$)
Simulation	(0, 1.0, 3.75)	895 µm	900 µm	890 µm	895 µm	N/A
	(0, 1.5, 5.70)	1250 µm	1260 µm	1260 µm	1260 µm	N/A
Experiment	(0, 1.0, 3.75)	1350 µm	1375 µm	1395 µm	1450 µm	N/A
	(0, 1.5, 5.70)	2505 µm	2475 µm	2550 µm	2625 µm	N/A
Simulation	(0, –1.0, 3.75)	N/A	900 µm	890 µm	890 µm	895 µm
	(0, –1.5, 5.70)	N/A	1260 µm	1260 µm	1265 µm	1260 µm
Experiment	(0, –1.0, 3.75)	N/A	1270 µm	1325 µm	1330 µm	1335 µm
	(0, –1.5, 5.70)	N/A	2355 µm	2450 µm	2525 µm	2615 µm

APPENDIX E: ELECTRIC-FIELD INTENSITY DISTRIBUTIONS ($|E|^2$) OF A SPIN-DECOUPLED METALENS AT LINE $z = 5.75$ mm ($x = 0$ mm)

The simulated and experimentally measured electric-field intensity distributions at line $z = 5.75$ mm ($x = 0$ mm) are shown in Fig. 8. For the incidence of LCP THz waves, one peak with normalized transmission $T = 0.615$ is observed at (0, 1.5, 5.75 mm) [see Figs. 8(a1) and 8(b1)]. Under the illumination of LECP ($\chi = 0.152$), LP ($\chi = 0$), and RECP ($\chi = -0.152$) THz waves, one more peak appears at (0, −1.5, 5.75 mm). The intensity ratios between these two peaks [at (0, 1.5, 5.75 mm) and (0, −1.5, 5.75 mm)] are about 0.58:0.42, 0.5:0.5, and 0.58:0.42, respectively [see Figs. 8(a2)–8(b4)]. For the incidence of RCP ($\chi = -1.0$)
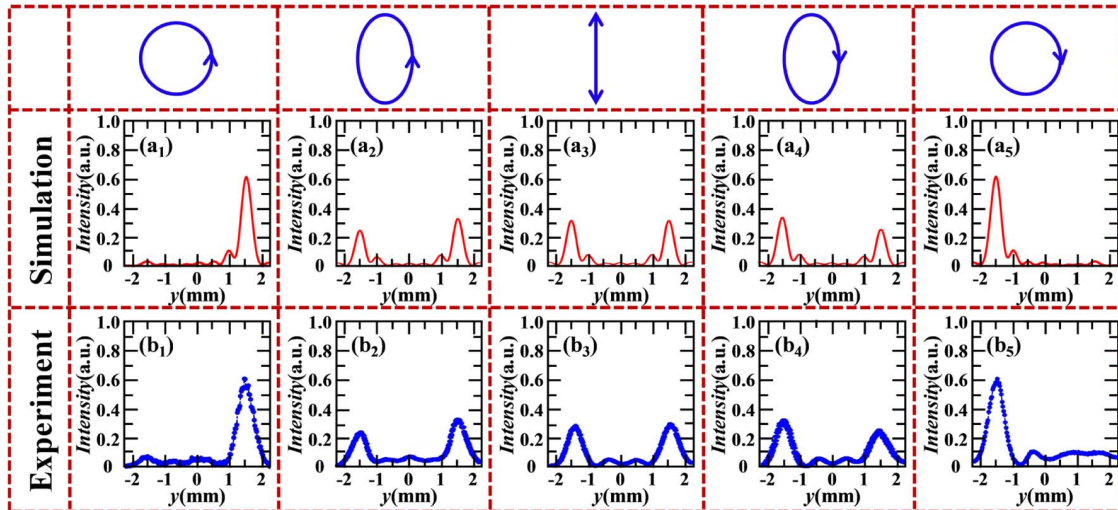

Fig. 8. Calculated and measured electric-field intensity distributions at line $z = 5.75$ mm ($x = 0$ mm), for the incidence of (a1), (b1) LCP, (a2), (b2) LECP, (a3), (b3) LP, (a4), (b4) RECP, and (a5), (b5) RCP THz waves, respectively.
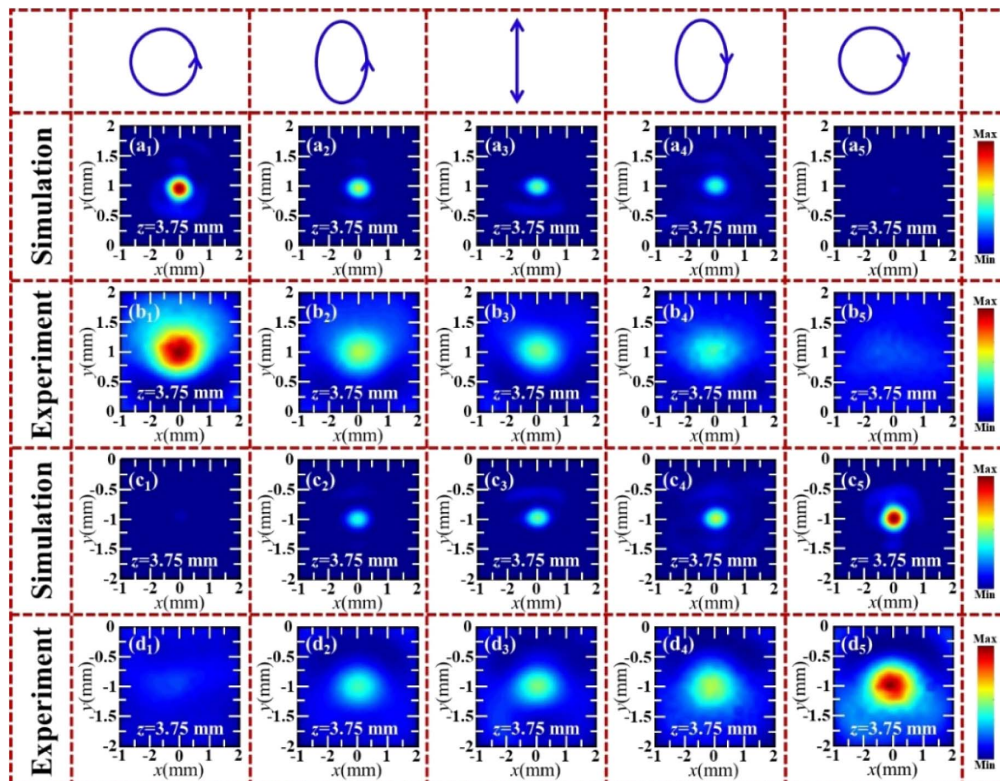

Fig. 9. Electric-field intensity distributions (under the illumination of THz waves with polarization switched from LCP to RCP) at the x – y plane ($z = 3.75$ mm) for the spin-decoupled metalens that can generate longitudinally distributed multiple focal points.

THz waves, the right peak disappears, leading to only one peak located at (0, –1.5, 5.75 mm). The normalized intensity for the right peak is about 0.615 as shown in Figs. 8(a5) and 8(b5). Therefore, the intensities of these two helicity-dependent focal points can be flexibly controlled by changing the ellipticity of the incident THz waves.

APPENDIX F: ELECTRIC-FIELD INTENSITY DISTRIBUTIONS ($|E|^2$) AT THE $x – y$ PLANE ($z = 3.75$ mm)

Figure 9 shows the electric-field intensity distributions of a spin-decoupled metalens (that can generate longitudinally distributed multiple focal points) when the polarization of incident THz waves is gradually switched from LCP to RCP. Under the illumination of LCP THz waves, one focal point is observed at (0, 1.0, 3.75 mm) [see Figs. 9(a1) and 9(b1)], while the focal point located at (0, –1.0, 3.75 mm) cannot be observed as shown in Figs. 9(c1) and 9(d1). When the ellipticity of the incident THz waves is switched to $\chi = 0.152$ (LECP), $\chi = 0$ (LP), or $\chi = –0.152$ (RECP), another focal point is observed at (0, –1.0, 3.75 mm) [see Figs. 9(a2)–9(d4)]. For the incidence of RCP THz waves, the focal point at (0, 1.0, 3.75 mm) disappears, and only a focal point located at (0, –1.0, 3.75 mm) can be observed as shown in Figs. 9(a5)–9(d5). In fact, when the polarization of incident THz waves is

gradually switched from LCP to RCP, the intensity of the upper focal point [at (0, 1.0, 3.75 mm)] gets weaker and weaker, while it becomes stronger and stronger for the focal point at (0, –1.0, 3.75 mm), demonstrating an intensity-tunable metalens.

APPENDIX G: ELECTRIC-FIELD INTENSITY DISTRIBUTIONS ($|E|^2$) AT THE $x – y$ PLANE ($z = 5.7$ mm)

For the spin-decoupled metalens that can generate longitudinally distributed multiple focal points, another one (or two) focal point(s) will be generated in the longitudinal direction as shown in Fig. 10. For the incidence of LCP THz waves, one focal point is observed at (0, 1.5, 5.7 mm), and none of focal points can be observed at (0, –1.5, 5.7 mm) [see Figs. 10(a1)–10(d1)]. Under the illumination of LECP ($\chi = 0.152$), LP ($\chi = 0$), or RECP ($\chi = –0.152$) THz waves, another focal point located at (0, –1.5, 5.7 mm) appears as shown in Figs. 10(a2)–10(d4). In contrast, only a focal point located at (0, –1.5, 5.7 mm) can be observed for the incidence of RCP THz waves [see Figs. 10(d1)–10(d5)]. The calculated and measured electric-field distributions in Fig. 10 also demonstrate that the designed spin-decoupled metalens enables intensity-tunable functionality between helicity-dependent focal points.
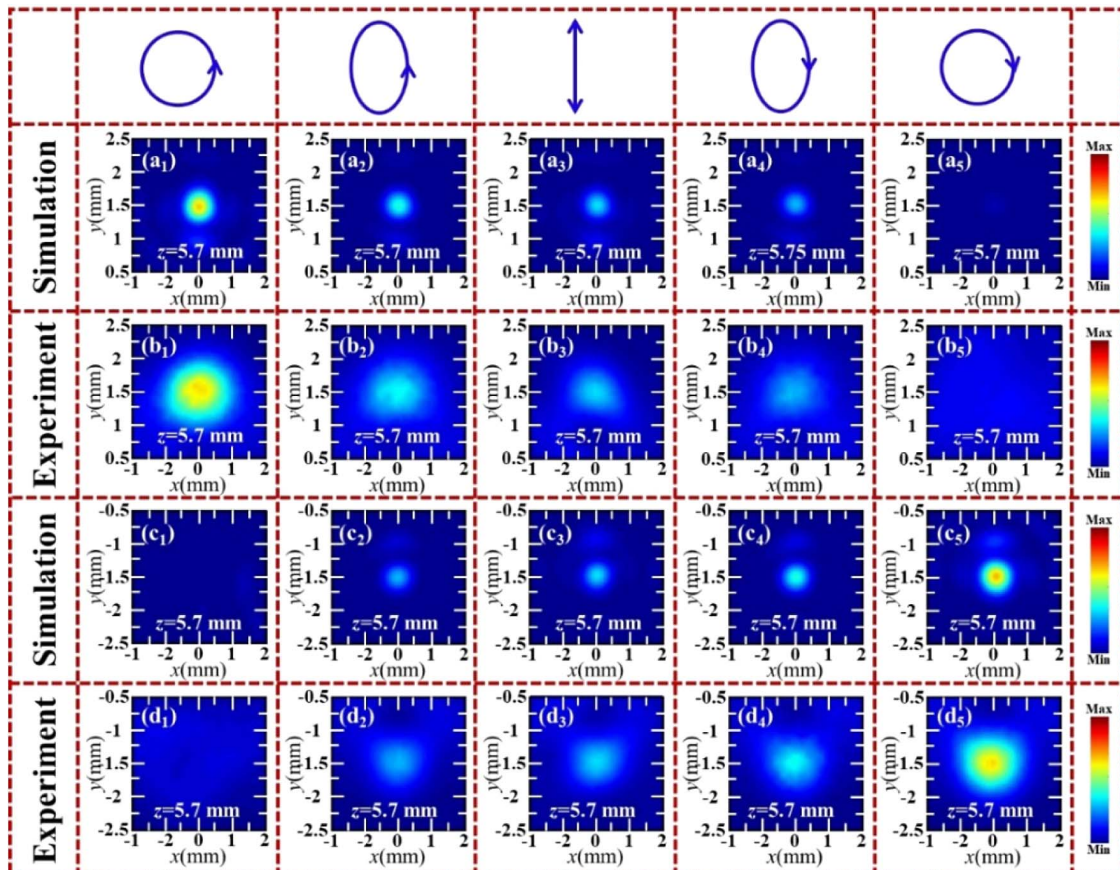

Fig. 10. Electric-field intensity distributions (under the illumination of THz waves with polarization switched from LCP to RCP) at the $x – y$ plane ($z = 5.7$ mm) for the spin-decoupled metalens that can generate longitudinally distributed multiple focal points.
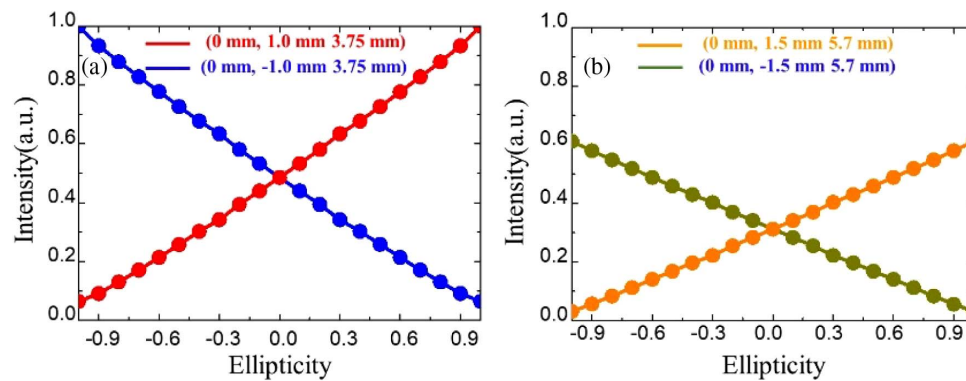
Fig. 11. Simulated electric-field intensities ($|E|^2$) at the focal plane. (a) The electric-field intensities ($|E|^2$) at point (0, 1.0, 3.75 mm) (red curve) and point (0, –1.0, 3.75 mm) (blue curve) with different ellipticity of THz waves. (b) The electric-field intensities ($|E|^2$) at point (0, 1.5, 5.7 mm) (orange curve) and point (0, –1.5, 5.7 mm) (dark yellow curve) with different ellipticity of the THz waves.

APPENDIX H: SIMULATED ELECTRIC-FIELD INTENSITIES ($|E|^2$) AT THE FOCAL PLANE

The calculated electric-field intensities of a spin-decoupled metalens (that can generate longitudinally distributed multiple focal points) at the focal plane are shown in Fig. 11. When the polarization of incident THz waves is gradually changed from LCP to RCP, the normalized intensity at (0, 1.0, 3.75 mm) [see the red curve in Fig. 11(a)] is decreased from 1 to 0, while the normalized intensity at (0, –1.0, 3.75 mm) is increased from 0 to 1 [see the blue curve in Fig. 11(a)]. The corresponding normalized electric-field intensity at point (0, 1.5, 5.7 mm) [or (0, –1.5, 5.7 mm)] is modulated from 0.615 to 0 (or 0 to 0.615) when the incident THz waves have polarization switched from LCP to RCP [see Fig. 11(b)]. In comparison with Figs. 11(a) and 11(b), we can conclude that the designed spin-decoupled metalens (that can generate longitudinally distributed multiple focal points) can enable the intensity-tunble functionality between the helicity-dependent focal points.

Disclosures. The authors declare no conflicts of interest.

REFERENCES

1. N. F. Yu, P. Genevet, M. A. Kats, F. Aieta, J. P. Tetienne, F. Capasso, and Z. Gaburro, "Light propagation with phase discontinuities: generalized laws of reflection and refraction," Science **334**, 333–377 (2011).
2. L. L. Huang, X. Z. Chen, H. Muhlenbernd, G. X. Li, B. F. Bai, Q. F. Tan, G. F. Jin, T. Zentgraf, and S. Zhang, "Dispersionless phase discontinuities for controlling light propagation," Nano Lett. **12**, 5750–5755 (2012).
3. X. J. Ni, N. K. Emani, A. V. Kildishev, A. Boltasseva, and V. M. Shalaev, "Broadband light bending with plasmonic nanoantennas," Science **335**, 427 (2012).
4. L. X. Liu, X. Q. Zhang, M. Kenney, X. Q. Sun, N. N. Xu, C. M. Ouyang, Y. L. Shi, J. G. Han, W. L. Zhang, and S. Zhang, "Broadband metasurfaces with simultaneous control of phase and amplitude," Adv. Mater. **26**, 5031–5036 (2015).
5. Z. C. Liu, Z. C. Li, Z. Liu, J. L. Li, H. Cheng, P. Yu, W. W. Liu, C. C. Tang, C. Z. Gu, J. L. Li, S. Q. Chen, and J. G. Tian, "High-performance broadband circularly polarized beam deflector by mirror effect of multinanorod metasurfaces," Adv. Funct. Mater. **25**, 5428–5434 (2015).
6. X. Chen, L. Huang, H. Mühlenbernd, G. Li, B. Bai, Q. Tan, G. Jin, C. Qiu, S. Zhang, and T. Zentgraf, "Dual-polarity plasmonic metalens for visible light," Nat. Commun. **3**, 1198 (2012).
7. X. Chen, M. Chen, M. Q. Mehmood, D. Wen, F. Yue, C. Qiu, and S. Zhang, "Longitudinal multifocimetalens for circularly polarized light," Adv. Opt. Mater. **3**, 1201–1206 (2015).
8. A. Arbabi, Y. Horie, M. Bagheri, and A. Faraon, "Dielectric metasurfaces for complete control of phase and polarization with subwavelength spatial resolution and high transmission," Nat. Nanotechnol. **10**, 937–943 (2015).
9. M. Khorasaninejad, W. T. Chen, R. C. Devlin, J. Oh, A. Y. Zhu, and F. Capasso, "Metalenses at visible wavelengths: diffraction-limited focusing and subwavelength resolution imaging," Science **352**, 1190–1194 (2016).
10. W. T. Chen, A. Y. Zhu, V. Sanjeev, M. Khorasaninejad, Z. J. Shi, E. Lee, and F. Capasso, "A broadband achromatic metalens for focusing and imaging in the visible," Nat. Nanotechnol. **13**, 220–226 (2019).
11. S. Wang, P. Wu, V. Su, Y. Lai, M. Chen, H. Kuo, B. Chen, Y. Chen, T. Huang, J. Wang, R. Lin, C. Kuan, T. Li, Z. Wang, S. Zhu, and D. Tsai, "A broadband achromatic metalens in the visible," Nat. Nanotechnol. **13**, 227–232 (2018).
12. R. J. Lin, V.-C. Su, S. Wang, M. K. Chen, T. L. Chung, Y. H. Chen, H. Y. Kuo, J.-W. Chen, J. Chen, Y.-T. Huang, J.-H. Wang, C. H. Chu, P. C. Wu, T. Li, Z. Wang, S. Zhu, and D. P. Tsai, "Achromatic metalens array for full-colour light-field imaging," Nat. Nanotechnol. **14**, 227–231 (2018).
13. X. Zang, H. Ding, Y. Intaravanne, L. Chen, Y. Peng, Q. Ke, A. V. Balakin, A. P. Shkurinov, X. Chen, Y. Zhu, and S. Zhuang, "A multi-foci metalens with polarization-rotated focal points," Laser Photon. Rev. **13**, 1900182 (2019).
14. X. Zang, W. Xu, M. Gu, B. Yao, L. Chen, Y. Peng, J. Xie, A. V. Balakin, A. P. Shkurinov, Y. Zhu, and S. Zhuang, "Polarization-insensitive metalens with extended focal depth and longitudinal high-tolerance imaging," Adv. Opt. Mater. **8**, 1901342 (2020).
15. X. J. Ni, A. V. Kildishev, V. M. Shalaev, and M. Vladimir, "Metasurface holograms for visible light," Nat. Commun. **4**, 2807 (2013).
16. L. L. Huang, X. Z. Chen, H. Muhlenbernd, H. Zhang, S. M. Chen, B. F. Bai, Q. F. Tan, G. F. Jin, K. W. Cheah, C. W. Qiu, J. Li, T. Zentgraf, and S. Zhuang, "Three-dimensional optical holography using a plasmonic metasurface," Nat. Commun. **4**, 2808 (2013).

17. Y. Yifat, M. Eitan, Z. Iluz, Y. Hanein, A. Boag, and J. Scheuer, "Highly efficient and broadband wide-angle holography using patch-dipole nanoantenna reflectarrays," Nano Lett. **14**, 2485–2490 (2014).

18. G. Zheng, H. Mühlenberd, M. Kenney, G. Li, T. Zentgraf, and S. Zhang, "Metasurface holograms reaching 80% efficiency," Nat. Nanotechnol. **10**, 308–312 (2015).

19. D. Wen, D. F. Yue, G. Li, G. Zheng, K. Chan, S. Chen, M. Chen, K. F. Li, P. W. H. Wong, K. W. Cheah, E. Y. B. Pun, S. Zhang, and X. Chen, "Helicity multiplexed broadband metasurface holograms," Nat. Commun. **6**, 8241 (2015).

20. Y. W. Huang, W. T. Chen, W. Tsai, P. Wu, C. Wang, G. Sun, and D. P. Tsai, "Aluminum plasmonic multicolor meta-hologram," Nano Lett. **15**, 3122–3127 (2015).

21. X. Li, L. W. Chen, Y. Li, X. H. Zhang, M. B. Pu, Z. Y. Zhao, X. L. Ma, Y. Q. Wang, M. H. Hong, and X. G. Luo, "Multicolor 3D meta-holography by broadband plasmonic modulation," Sci. Adv. **2**, e1601102 (2016).

22. Z. J. Yue, G. L. Xue, J. Liu, Y. T. Wang, and M. Gu, "Nanometric holograms based on a topological insulator material," Nat. Commun. **8**, 15354 (2017).

23. L. Jin, Z. Dong, S. Mei, Y. Yu, Z. Wei, Z. Pan, S. Rezaei, X. Li, A. I. Kuznetsov, Y. S. Kivshar, J. K. W. Yang, and C. W. Qiu, "Noninterleaved metasurface for (2^6−1) spin- and wavelength-encoded holograms," Nano Lett. **18**, 8016–8024 (2018).

24. Y. Wang, C. Guan, H. Li, X. Ding, K. Zhang, J. Wang, S. N. Burokur, J. Liu, and Q. Wu, "Dual-polarized tri-channel encrypted holography based on geometric phase metasurface," Adv. Photon. Res. **1**, 2000022 (2020).

25. X. B. Yin, Z. L. Ye, J. Rho, Y. Wang, and X. Zhang, "Photonic spin Hall effect at metasurfaces," Science **339**, 1405–1407 (2013).

26. X. H. Ling, X. X. Zhou, X. N. Yi, W. X. Shu, Y. C. Liu, S. Z. Chen, H. L. Luo, S. C. Wen, and D. Y. Fan, "Giant photonic spin Hall effect in momentum space in a structured metamaterial with spatially varying birefringence," Light Sci. Appl. **4**, e290 (2015).

27. W. J. Luo, S. Y. Xiao, Q. He, S. L. Sun, and L. Zhou, "Photonic spin Hall effect with nearly 100% efficiency," Adv. Opt. Mater. **3**, 1102–1108 (2015).

28. X. F. Zang, B. S. Yao, Z. Li, Y. Zhu, J. Y. Xie, L. Chen, A. V. Balakin, A. P. Shkurinov, Y. M. Zhu, and S. L. Zhuang, "Geometric phase for multidimensional manipulation of photonics spin Hall effect and helicity-dependent imaging," Nanophotonics **9**, 1501–1508 (2020).

29. N. K. Grady, J. E. Heyes, D. R. Chowdhury, Y. Zeng, M. T. Reiten, A. K. Azad, A. J. Taylor, D. A. Dalvit, and H. T. Chen, "Terahertz metamaterials for linear polarization conversion and anomalous refraction," Science **340**, 1304–1307 (2013).

30. N. Yu, F. Aieta, P. Genevet, M. A. Kats, Z. Gaburro, and F. Capasso, "A broadband, background-free quarter-wave plate based on plasmonicmetasurfaces," Nano Lett. **12**, 6328–6333 (2012).

31. R. Fan, Y. Zhou, X. Ren, R. Peng, S. Jiang, D. Xu, X. Xiong, X. Huang, and M. Wang, "Freely tunable broadband polarization rotator for terahertz waves," Adv. Mater. **27**, 1201–1206 (2015).

32. X. F. Zang, H. H. Gong, Z. Li, J. Y. Xie, Q. Q. Cheng, L. Chen, A. P. Shkurinov, Y. M. Zhu, and S. L. Zhuang, "Metasurface for multi-channel terahertz beam splitters and polarization rotators," Appl. Phys. Lett. **112**, 171111 (2018).

33. M. B. Pu, X. Li, X. L. Ma, Y. Q. Wang, Z. Y. Zhao, C. T. Wang, C. G. Hu, P. Gao, C. Huang, H. R. Ren, X. P. Li, F. Qin, J. Yang, M. Gu, M. H. Hong, and X. G. Luo, "Catenary optics for achromatic generation of perfect optical angular momentum," Sci. Adv. **1**, e1500396 (2015).

34. M. Q. Mehmood, S. T. Mei, S. Hussain, K. Huang, S. Y. Siew, L. Zhang, T. H. Zhang, X. H. Ling, H. Liu, J. H. Teng, A. Danner, S. Zhang, and C. W. Qiu, "Visible-frequency metasurface for structuring and Spatially multiplexing optical vortices," Adv. Mater. **28**, 2533–2539 (2016).

35. F. Yue, D. Wen, C. Zhang, B. D. Gerardot, W. Wang, S. Zhang, and X. Chen, "Multichannel polarization-controllable superpositions of orbital angular momentum states," Adv. Mater. **29**, 1603838 (2017).

36. X. Zang, Y. Zhu, C. Mao, W. Xu, H. Ding, J. Xie, Q. Cheng, L. Chen, Y. Peng, Q. Hu, M. Gu, and S. Zhuang, "Manipulating terahertz plasmonic vortex based on geometric and dynamic phase," Adv. Opt. Mater. **7**, 1801328 (2018).

37. Y. J. Bao, J. C. Ni, and C. W. Qiu, "A minimalist single-layer metasurface for arbitrary and full control of vector vortex beams," Adv. Mater. **32**, 1905659 (2020).

38. G. X. Li, S. M. Chen, N. Pholchai, B. Reineke, P. W. H. Wong, E. Y. B. Pun, K. W. Cheah, T. Zentgraf, and S. Zhang, "Continuous control of the nonlinearity phase for harmonic generations," Nat. Mater. **14**, 607–612 (2015).

39. E. Almeida, O. Bitto, and Y. Prior, "Nonlinear metamaterialss for holography," Nat. Commun. **7**, 12533 (2016).

40. F. Walter, G. X. Li, C. Meier, S. Zhang, and T. Zentgraf, "Ultrathin nonlinear metasurface for optical image encoding," Nano Lett. **17**, 3171–3176 (2017).

41. T. Komine and M. Nakagawa, "Fundamental analysis for visible-light communication system using LED lights," IEEE Trans. Consum. Electron. **50**, 100–107 (2004).

42. K. Modepalli and L. Parasa, "Dual-purpose offline LED driver for illumination and visible light communication," IEEE Trans. Ind. Appl. **51**, 406–419 (2015).

43. W. W. Liu, Z. C. Li, Z. Li, H. Cheng, C. C. Tang, J. J. Li, S. Q. Chen, and J. G. Tian, "Energy tailorable spin-selective multifunctional metasurfaces with full Fourier components," Adv. Mater. **31**, 1901729 (2019).

44. L. Bao, R. Y. Wu, X. J. Fu, Q. Ma, G. D. Bai, J. Mu, R. Z. Jiang, and T. J. Cui, "Multi-beam forming and controls by metasurface with phase and amplitude modulations," IEEE Trans. Anntenas Propag. **67**, 6680–6685 (2019).

45. Z. X. Shen, S. H. Zhou, S. J. Ge, W. Duan, L. L. Ma, Y. Q. Lu, and W. Hu, "Liquid crystal tunable terahertz lens with spin-selected focusing property," Opt. Express **27**, 8800–8807 (2019).

46. H. R. Lv, X. Q. Lu, Y. S. Han, M. Zhen, and S. Y. Teng, "Multifocal metalens with a controllable intensity ratio," Opt. Lett. **44**, 2518–2521 (2019).

47. G. W. Ding, K. Chen, G. X. Qian, J. M. Zhao, T. Jiang, Y. J. Feng, and Z. B. Wang, "Independent energy allocation of dual-helical multibeams with spin-selective transmissive metasurface," Adv. Opt. Mater. **8**, 200342 (2020).

48. Y. H. Xu, Q. Li, X. Q. Zhang, M. G. Wei, Q. Xu, Q. Wang, H. F. Zhang, W. T. Zhang, C. Hu, Z. W. Zhang, C. L. Zhang, X. X. Zhang, J. G. Han, and W. L. Zhang, "Spin-decoupled multifunctional metasurface for asymmetric polarization generation," ACS Photon. **6**, 2933–2941 (2019).

49. Y. Y. Yuan, S. Sun, Y. Chen, K. Zhang, X. M. Ding, B. Ratni, Q. Wu, S. N. Burokur, and C. W. Qiu, "A fully phase-modulated metasurface as an energy-controllable circular polarization router," Adv. Sci. **7**, 2001437 (2020).

50. B. H. Chen, P. C. Wu, V. C. Su, Y. C. Lai, C. H. Chu, C. Lee, J. W. Chen, Y. H. Chen, Y. C. Lan, C. H. Kuan, and D. P. Tsai, "GaN metalens for pixel-level full-color routing at visible light," Nano Lett. **17**, 6345–6352 (2017).

51. J. P. B. Mueller, N. A. Rubin, R. C. Devlin, B. Groever, and F. Capasso, "Metasurface polarization optics: independent phase control of arbitrary orthogonal states of polarization," Phys. Rev. Lett. **118**, 113901 (2017).

52. L. Z. Yin, T. J. Huang, F. Y. Han, J. Y. Liu, D. Wang, and P. K. Liu, "High-efficiency terahertz spin-decoupled meta-coupler for spoof surface plasmon excitation and beam steering," Opt. Express **27**, 18928–18939 (2019).

53. L. Tang, R. Jin, Y. Cao, J. Li, J. Wang, and Z. G. Dong, "Spin-dependent dual-wavelength multiplexing metalens," Opt. Lett. **45**, 5258–5261 (2020).

54. B. Wang, F. Dong, H. Feng, D. Yang, Z. Song, L. Xu, W. Chu, Q. Gong, and Y. Li, "Rochon-prism-like planar circularly polarized beam splitters based on dielectric metasurfaces," ACS Photon. **5**, 1660–1664 (2018).

55. Y. Xu, Q. Li, X. Zhang, M. Wei, Q. Xu, Q. Wang, H. Zhang, W. Zhang, C. Hu, Z. Zhang, C. Zhang, X. Zhang, J. Han, and W. Zhang, "Spin-decoupled multifunctional metasurface for asymmetric polarization generation," ACS Photon. **6**, 2933–2941 (2019).

56. H. X. Xu, G. Hu, Y. Li, L. Han, J. Zhao, Y. Sun, F. Yuan, G. M. Wang, Z. H. Jiang, X. Ling, T. J. Cui, and C. W. Qiu, "Interference-assisted kaleidoscopic meta-plexer for arbitrary spin-wavefront manipulation," Light Sci. Appl. **8**, 3 (2019).

57. Y. Yuan, K. Zhang, X. Ding, B. Ratni, S. N. Burokur, and Q. Wu, "Complementary transmissive ultra-thin meta-deflectors for broadband polarization-independent refractions in the microwave region," Photon. Res. **7**, 80–88 (2019).

58. G. Ding, K. Chen, X. Luo, J. Zhao, T. Jiang, and Y. Feng, "Dual-helicity decoupled coding metasurface for independent spin-to-orbital angular momentum conversion," Phys. Rev. Appl. **11**, 044043 (2019).

59. K. Zhang, Y. Yuan, X. Ding, B. Ratni, S. N. Burokur, and Q. Wu, "High-efficiency metalenses with switchable functionalities in microwave region," ACS Appl. Mater. Interfaces **11**, 28423–28430 (2019).

60. K. Zhang, Y. Yuan, X. Ding, H. Li, B. Ratni, Q. Wu, J. Liu, S. N. Burokur, and J. Tan, "Polarization-engineered noninterleaved meta-surface for integer and fractional orbital angular momentum multiplexing," Laser Photon. Rev. **15**, 2000351 (2020).

61. S. Boroviks, R. A. Deshpande, N. A. Mortensen, and S. I. Bozhevolnyi, "Multifunctional metamirror: polarization splitting and focusing," ACS Photon. **5**, 1648–1653 (2018).

62. X. Yin, H. Zhu, H. Guo, M. Deng, T. Xu, Z. Gong, X. Li, Z. H. Hang, C. Wu, H. Li, S. Chen, L. Zhou, and L. Chen, "Hyperbolic metamaterial device for wavefront manipulation," Laser Photon. Rev. **13**, 1800081 (2019).

63. C. Chen, S. Gao, W. Song, H. Li, S. N. Zhu, and T. Li, "Metasurfaces with planar chiral meta-atoms for spin light manipulation," Nano Lett. **21**, 1815–1821 (2021).

64. Y. Yuan, K. Zhang, B. Ratni, Q. Song, X. Ding, Q. Wu, S. N. Burokur, and P. Genevet, "Independent phase modulation for quadruplex polarization channels enabled by chirality-assisted geometric-phase metasurfaces," Nat. Commun. **11**, 4186 (2020).

65. Y. Chen, X. Yang, and J. Gao, "Spin-controlled wavefront shaping with plasmonic chiral geometric metasurfaces," Light Sci. Appl. **7**, 84 (2018).